Journal of Molecular Spectroscopy **201,** 116–123 (2000)
doi:10.1006/jmsp.2000.8076, available online at http://www.idealibrary.com on IDEAL®

High-Resolution Laser Spectroscopy of the $\tilde{A}^2B_2$–$\tilde{X}^2A_1$ and $\tilde{B}^2B_1$–$\tilde{X}^2A_1$ Systems of $SrNH_2$

C. R. Brazier[1] and P. F. Bernath[2]

Department of Chemistry, University of Arizona, Tucson, Arizona 85721

Received October 28, 1999; in revised form January 21, 2000

The 0_0^0 bands of the $\tilde{A}^2B_2$–$\tilde{X}^2A_1$ and $\tilde{B}^2B_1$–$\tilde{X}^2A_1$ systems of $SrNH_2$ were observed at Doppler-limited resolution using a Broida oven source and laser-induced fluorescence detection. A full rotational analysis of both transitions was performed including K_a levels up to 5 and J levels up to 55. The $\tilde{B}^2B_1$ state was found to be extensively perturbed and only some of the subbands could be analyzed. The $\tilde{A}^2B_2$ and $\tilde{B}^2B_1$ states undergo a strong Coriolis-type interaction which results in extremely large spin–rotation splittings in both states, effectively splitting all levels with $K_a' \neq 0$ into two well-separated spin components.

INTRODUCTION

There have been a considerable number of studies of pseudo-halide derivatives of calcium and strontium in recent years. These were recently reviewed by Bernath (*1, 2*). The initial high-resolution studies of linear species such as halides and hydroxides were more recently extended to lower symmetry species such as the C_{3v} methyl (*3*) and methoxide (*4, 5*) derivatives. Recently the bent CaSH molecule which has C_s symmetry was analyzed (*6, 7*).

The only C_{2v} derivative to be analyzed at high resolution so far is $CaNH_2$, which was first observed by Wormsbecher *et al.* (*8, 9*). They recorded the chemiluminescent emission from the reaction of calcium, strontium, and barium vapors with hydrazine. The spectra, which were also observed when ammonia was used, were interpreted as arising from the alkaline–earth monoamide molecules MNH_2. They performed a rotational analysis of a single subband of the $\tilde{C}^2A_1$–$\tilde{X}^2A_1$ system of $CaNH_2$ (*9*). Further studies of jet-cooled $CaNH_2$ were carried out by Whitham *et al.* (*10, 11*) resulting in a partial rotational analysis of the $\tilde{B}^2B_1$–$\tilde{X}^2A_1$ and $\tilde{A}^2B_2$–$\tilde{X}^2A_1$ systems. The $\tilde{A}^2B_2$ and $\tilde{B}^2B_1$ electronic states have a strong mutual interaction, and they explained the effects in terms of a second-order perturbation between the two states based on the spin–orbit and Coriolis-coupling terms. Recently several high-resolution studies of $CaNH_2$ were carried out. Marr *et al.* (*12*) recorded the $\tilde{A}^2B_2$–$\tilde{X}^2A_1$ system and performed the first full-rotational analysis of $CaNH_2$. They also determined the ground state dipole moment to be 1.74 D using optical Stark spectroscopy. The $\tilde{B}^2B_1$–$\tilde{X}^2A_1$ system has been observed by Morbi *et al.* (*13*) and the $\tilde{C}^2A_1$–$\tilde{X}^2A_1$ system by Morbi *et al.* (*14*).

The electronic states for the alkaline–earth pseudohalides are well described by a simple ionic model where the ligand has a negative charge and one unpaired electron remains on the positively charged metal atom. In the ground state the unpaired electron is in a predominantly *s* orbital that is polarized away from the negatively charged ligand by mixing in some *p* and *d* character. Strong electronic transitions occur to excited states having an unpaired electron in a predominantly *p* orbital, which is also polarized away from the ligand by mixing in some *d* character. As the symmetry of the molecule is reduced from spherical to linear in the halides, the ^2P state splits into $^2\Pi$ and $^2\Sigma^+$ electronic states. In C_{2v} symmetry the $^2\Pi$ state is split into $^2B_2$ and $^2B_1$ states. These simple explanations were confirmed by electron propagator calculations for many of the calcium species including $CaNH_2$ by Ortiz (*15*).

In their study of the chemiluminescent reactions of alkaline–earth metals, Wormsbecher *et al.* (*8*) reported the first spectrum of $SrNH_2$. They observed three bands between 6300 and 7000 Å which they attributed to transitions between the $\tilde{A}^2B_2$, $\tilde{B}^2B_1$, and $\tilde{C}^2A_1$ states and the $\tilde{X}^2A_1$ ground state. Low-resolution laser-induced fluorescence spectra and approximate band centers and some vibrational frequencies for $SrNH_2$ were reported by Bopegedera *et al.* (*16*).

At the beginning of this investigation, spectra of the $\tilde{B}^2B_1$–$\tilde{X}^2A_1$ system were recorded at high resolution as the wavelength region was more readily accessible. As the different subbands were examined, it became clear that many of them were perturbed from their expected positions. To obtain a full analysis without the complication of perturbations, the $\tilde{A}^2B_2$–$\tilde{X}^2A_1$ system was recorded. We report here a full analysis of the $\tilde{A}^2B_2$–$\tilde{X}^2A_1$ system of $SrNH_2$ and a partial analysis of those

Supplementary data for this article are available on the journal home page (http://www.academicpress.com/jms) and as part of the Ohio State University Molecular Spectroscopy Archives (http://msa.lib.ohio-state.edu/jmsa_hp.htm).

[1] Current address: Department of Chemistry, CSU San Bernardino, San Bernardino, CA 92407-2397.

[2] Also associated with Department of Chemistry, University of Waterloo, Waterloo, Ontario, Canada N2L 3G1.

0022-2852/00 $35.00

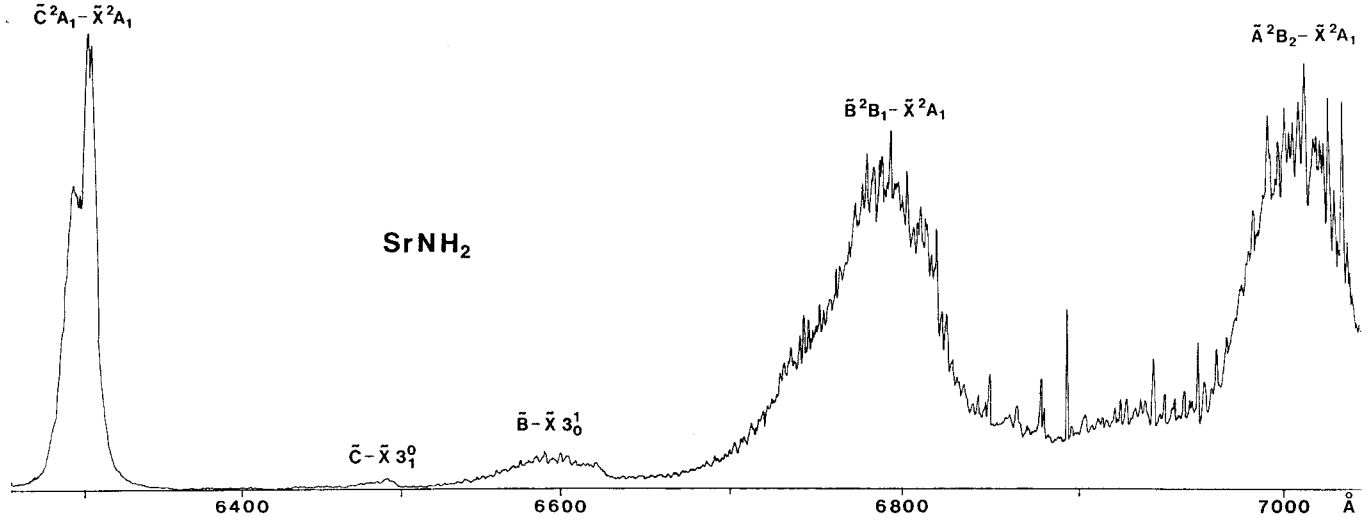

FIG. 1. Low-resolution (1 cm^{-1}) scan of the $\tilde{A}^2B_2$–$\tilde{X}^2A_1$, $\tilde{B}^2B_1$–$\tilde{X}^2A_1$, and $\tilde{C}^2A_1$–$\tilde{X}^2A_1$ systems of $SrNH_2$. The red-most transitions show the characteristic open structure of perpendicular bands for an asymmetric top, while the 6300 Å feature is clearly a parallel band. Several features associated with the ν_3 Sr–N stretching vibration were also seen.

subbands in the $\tilde{B}^2B_1$–$\tilde{X}^2A_1$ system which were not significantly perturbed.

EXPERIMENTAL

Strontium monoamide was produced in a Broida-type oven (*17*) by the reaction of strontium vapor with ammonia. Strontium metal was resistively heated in an alumina crucible and the vapor entrained in a flow of argon carrier gas. The total pressure was typically 2 Torr of argon and a few mTorr of ammonia with a slow flow through the system.

Two cw dye lasers were used to obtain the spectra. A broadband (1 cm^{-1}) CR599-01 dye laser pumped by a Coherent Innova 90 argon ion laser was used to excite the $^3P_1$–^1S strontium atomic line. This resulted in a large increase in the formation of $SrNH_2$. A single-frequency (1 MHz) CR699-29 ring laser pumped by a Coherent Innova 20-argon ion laser was used to record the high-resolution spectra. DCM and LD688 dyes were used as appropriate. The two beams were focused colinearly into the oven but were not precisely overlapped. The fluorescence from only the probe beam was focused onto the entrance slit of a 0.64-m monochromator. The dispersed fluorescence was imaged onto an RCA C31034 phototube and after processing through photon-counting electronics recorded as a function of laser frequency using the Coherent autoscan system. The monochromator acted as a narrow band filter to simplify the spectrum by recording only lines from the subband of interest. Calibration of the autoscan system was checked at least once each day by recording a section of the iodine spectrum and comparing this with the published line positions (*18, 19*). By this method the relative positions of unblended lines could be determined to a precision of 0.003 cm^{-1}. The absolute accuracy is limited by the iodine atlas to about 0.005 cm^{-1}.

VIBRATIONAL ANALYSIS

Low-resolution laser excitation spectra were recorded by scanning a broadband dye laser through the region where chemiluminescence was observed (*8*) and monitoring the fluorescence through a red-pass filter which blocked the laser. The spectrum, which is shown in Fig. 1, consisted of three main bands and several weaker features which were attributed to vibrations. The two bands to the red have the open structure characteristic of perpendicular transitions in an asymmetric rotor, while the highest frequency transition has the narrow profile of a parallel band. A list of the approximate band centers and vibrational frequencies is given in Table 1.

The $SrNH_2$ molecule has six vibrational modes. Three of these (ν_1, ν_2, and ν_3) are totally symmetric and hence are allowed in one quantum. They are represented by the symmet-

TABLE 1

Band Centers and Vibrational Frequencies for $SrNH_2$ (in cm^{-1})

$\tilde{A}^2B_2$–$\tilde{X}^2A_1$ **14274**

$\tilde{B}^2B_1$–$\tilde{X}^2A_1$ **14724**

$\tilde{C}^2A_1$–$\tilde{X}^2A_1$ **15862**

Mode	Motion	$\tilde{X}^2A_1$	$\tilde{B}^2B_1$	$\tilde{C}^2A_1$
ν_1	N-H symmetric stretch	3293±10		
ν_2	NH_2 bend	1678±10		
ν_3	Sr-N stretch	459±5	444±5	458±5
ν_4	Out of plane Sr-N-H bend	320±30		290±30
ν_5	N-H asymmetric stretch			
ν_6	In plane Sr-N-H bend	320±30		290±30

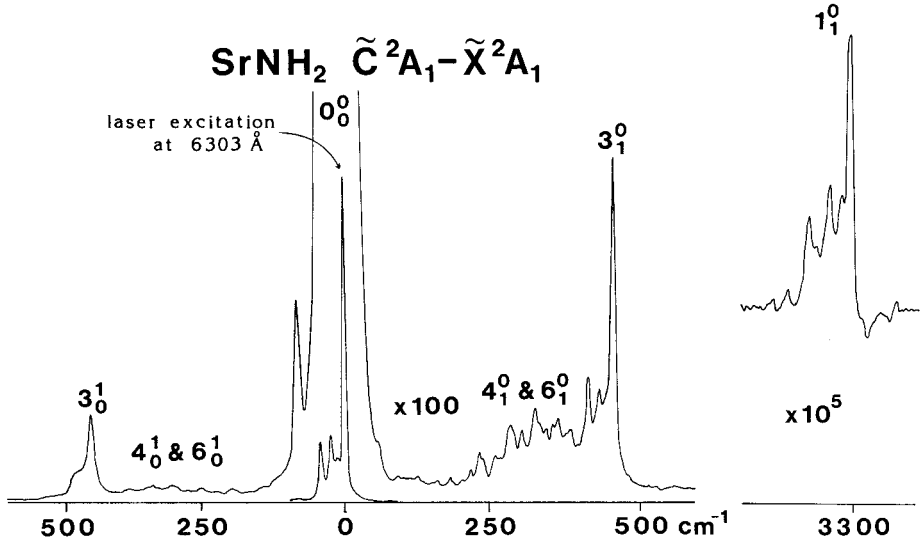

FIG. 2. Resolved fluorescence spectrum obtained by exciting the strongest feature in the $\tilde{C}^2A_1$–$\tilde{X}^2A_1$ system of $SrNH_2$. The strongest emission is observed for the ν_3 vibration. The vibronically allowed ν_4 and ν_6 modes are seen weakly (the observed feature may be due to either or both bands). The ν_1 band is seen very weakly (note the changes in scale) but with identical rotational structure. In this scan the ν_2 band was obscured by nonresonant emission from the $\tilde{A}^2B_2$–$\tilde{X}^2A_1$ system.

ric N–H stretch, the NH_2 bend, and the Sr–N stretch, respectively. As the electronic transition is centered on the metal, only the Sr–N stretch is expected to be strong, and this is indeed the case. The three bending modes, $\nu_4(b_1)$, the out-of-plane deformation; $\nu_5(b_2)$, the asymmetric NH_2 stretch; and $\nu_6(b_2)$, the in-plane Sr–N–H bend; are all forbidden in one quantum.

The ground state vibrational frequencies were determined by fixing the excitation laser on a single strong feature and dispersing the fluorescence. Several of the bandheads in the $\tilde{A}^2B_2$–$\tilde{X}^2A_1$ band were examined as well as the $\tilde{C}^2A_1$–$\tilde{X}^2A_1$ band. Part of a dispersed fluorescence spectrum for the $\tilde{C}^2A_1$–$\tilde{X}^2A_1$ band is shown in Fig. 2. Dispersed fluorescence spectra from the $\tilde{B}^2B_1$ state were obscured by relaxed emission from the $\tilde{A}^2B_2$ state.

The 3_1^0 band was strong in all of the spectra, with an estimated Franck–Condon factor of about 0.04. The relative intensities are approximate and no attempt has been made to correct for variations in monochromator efficiency or detector response. The 3_2^0 and 3_3^0 bands were also observed, with each weaker by approximately the same ratio. There was only a slight change in frequency for each quantum, indicating very little anharmonicity in the potential. This is typical for the strontium pseudohalides; for example, the anharmonicity for the Sr–O stretch was found to be 8 cm^{-1} in SrOH (*20*).

The two symmetric NH_2 modes, the stretch (ν_1) and the bend (ν_2), were both seen weakly, but reproducibly, in several spectra. The rotational pattern was the same as for the excitation band, indicating resonant excitation of the same group of rotational levels. The Franck–Condon factors were both extremely small, about 4×10^{-5} and 2×10^{-5}, respectively. The observed frequencies are both somewhat higher than in the free-amide anion (c.f., 3122 and 1463 cm^{-1}) and the NH_2 radical (c.f., 3219 and 1497 cm^{-1}).

Weak bands around 320 cm^{-1} were also observed for dispersed fluorescence spectra from the $\tilde{C}^2A_1$ state. These are tentatively assigned to the Sr–N–H in- and out-of-plane bending modes ν_6 and ν_4. The bands are fairly broad and it is not possible to assign separate features for 4_1^0 and 6_1^0. Both bands are likely to have similar frequencies and the single broad band most likely arises from a mix of the two bands. Both of these vibrations are formally forbidden in one quantum but become allowed due to vibronic coupling of the $\tilde{C}^2A_1$ state with the nearby $\tilde{A}^2B_2$ and $\tilde{B}^2B_1$ states. Similar forbidden vibrations were observed in the isoelectronic SrOH molecule (*20*).

The 3_0^1 Sr–N stretching vibrations were observed for the $\tilde{C}^2A_1$ and $\tilde{B}^2B_1$ states in the laser excitation spectra. The frequencies are little changed from the ground state. The 3_0^1 band for the $\tilde{A}^2B_2$ state is at essentially the same energy as the origin of the $\tilde{B}^2B_1$–$\tilde{X}^2A_1$ system.

ROTATIONAL ANALYSIS

The first transition of $SrNH_2$ to be rotationally analyzed was the $\tilde{B}^2B_1$–$\tilde{X}^2A_1$ system at 6790 Å. The low-resolution spectrum (1 cm^{-1}) in Fig. 1 contains many sharp features which are likely to be bandheads. This was confirmed by scanning across them at Doppler-limited resolution (0.03 cm^{-1}). The clearest bandheads in the $\tilde{B}$–$\tilde{X}$ transition are to the red of the center of the transition, suggesting that the expected vibrational sequence structure is shifted somewhat to the blue of the 0_0^0 band.

The first feature to be examined was the strong clear band-

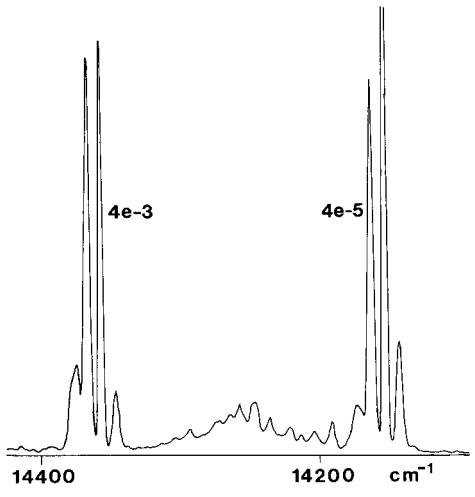

FIG. 3. A typical example of a dispersed fluorescence spectrum used to identify the K_a assignment of bandheads. The $-1B$ bandhead of the 4–5 ("e" or F_2) subband of the $\tilde{A}^2B_2$–$\tilde{X}^2A_1$ system of $SrNH_2$ is excited. Emission from the 4–3 subband 16 A'' to the blue confirms the K_a assignment. The presence of four features in each group of lines confirms the Hund's case (a)–(b) nature of the transition. The extra structure between the two bands is due to other overlapping transitions that were also excited by the laser.

head at 6849 Å (14 595 cm^{-1}). When the bandhead was excited by the laser and the fluorescence dispersed through a monochromator, a spectrum similar to that shown in Fig. 3 was observed. (The original spectra were not preserved; Fig. 3 is actually from the $\tilde{A}^2B_2$–$\tilde{X}^2A_1$ system.) Two sets of four lines were observed with the center lines being much stronger than the outer ones. The splitting into two groups was exactly as expected. The $\tilde{B}^2B_1$–$\tilde{X}^2A_1$ system of $SrNH_2$ is a perpendicular transition and has a selection rule of $\Delta K_a = \pm 1$. Hence when a particular K_a level in the $\tilde{B}$ state is excited, emission occurs back to the two ground state K_a levels to which it is connected. If an approximate value for the A rotational constant is available, then the splitting between the two bands gives the K_a assignment for the transition.

The splitting into four lines for each component was not expected, however. All of the subbands for a perpendicular transition of an asymmetric rotor would normally be expected to exhibit a strong Q branch and weaker P and R branches. Hence excitation of a single bandhead, most likely a Q branch, would give rise to a triplet for each subband, with the central Q feature stronger than the accompanying P and R transitions. The pattern of four lines was, however, exactly the same as had been seen for the isoelectronic linear molecules, such as SrOH (*20*). The $\tilde{A}^2\Pi$–$\tilde{X}^2\Sigma^+$ transition of SrOH is a Hund's case (a) $^2\Pi$ to case (b) $^2\Sigma^+$ band. The excited state rotational levels are given by $B'J(J+1)$ and the ground state levels by $B''N(N+1)$, where J is half-integer and N integer. If the rotational constants are fairly similar, then branches spaced by $-3B$, $-B(2)$, $+B(2)$, and $+3B$ occur for each spin–orbit component. Hence, excitation of one feature gives rise to a quartet in emission with the central features much stronger than the outer ones. This implies that the coupling case in the $\tilde{B}^2B_1$ state of $SrNH_2$ is equivalent to Hund's case (a) for a linear molecule. That is, the electron spin in the excited state is coupled to the a-rotational axis of the molecule. This results in a large effective spin–rotation interaction (ϵ_{aa}) in the $\tilde{B}^2B_1$ state. Each subband with $K_a \geq 1$ in the upper state is then split into two components separated by $\epsilon_{aa}K_a$. In the absence of asymmetry doubling, each pair of bands would correspond to a case (a)–case (b) transition for a linear molecule with the K_a quantum number corresponding to Λ in the linear case. Hence the pair of subbands observed in the initial scan, 2–3 and 2–1, correspond to one spin component of case (a) to case (b) $^2\Delta$–$^2\Phi$ and $^2\Delta$–$^2\Pi$ transitions, respectively.

Recording of the full-rotational structure for the subbands was relatively straightforward. As the two sets of emission peaks corresponding to $\Delta K_a = +1$ and -1 were widely separated, it was possible to open the slits on the monochromator and record emission in one subband while scanning through the other. The $-B$ branches reach bandheads at moderate J so it was possible to record all of the rotational levels from the origin to J of about 40 simultaneously. A section from a scan of this type is shown in Fig. 4. Since first lines were observed in all of the branches, assignment of the lines was relatively easy. The first lines in the upper state had $J = 2.5$ or $K_a + \frac{1}{2}$, hence the first bands recorded correspond to the "e" spin component. As these bands are on the extreme red side of the $\tilde{B}^2B_1$–$\tilde{X}^2A_1$ transition, they are likely to involve the lower or F_1 spin component. The corresponding "f" (or F_2) component is expected to lie much higher. The $\tilde{B}^2B_1$–$\tilde{X}^2A_1$ bands are equivalent to a set of case (a) inverted to case (b) transitions for a linear molecule. The 2–3e band showed no sign of asymmetry splitting, indicating that the splitting in the upper state 2e level is extremely small. The 2–1e band showed a large splitting due to the $K_a = 1$ level in the ground state. The 2–1f and 2–3f bands were then analyzed. These were separated by 64 cm^{-1} from the 2–1e and 2–3e bands corresponding to an effective spin–rotation splitting $\epsilon_{aa} = 32$ cm^{-1}. The $K_a = 2f$ levels were found to exhibit a large asymmetry doubling, indicating that the spin–rotation and rotation contributions to the asymmetry splittings are comparable, resulting in large splittings in one component and small ones in the other.

The first bands observed are among the strongest in the $\tilde{B}^2B_1$–$\tilde{X}^2A_1$ system as they involve low odd K_a levels. The $SrNH_2$ molecule has two equivalent protons which results in *ortho* and *para* forms with a 3:1 intensity ratio. In the $\tilde{X}^2A_1$ state the K_a odd levels occur only for the *ortho* form and K_a even only for *para* form.

The positions of the other low K_a subbands were predicted and several were recorded. However, the 1–0f and 1–2f bands could not be found, despite an extensive search. The 0–1 subband which, as the excited state K_a is zero is not split into two components by the spin–rotation interaction, also could not be found where it was predicted. These and several higher K_a subbands of the $\tilde{B}^2B_1$–$\tilde{X}^2A_1$ system either could not be

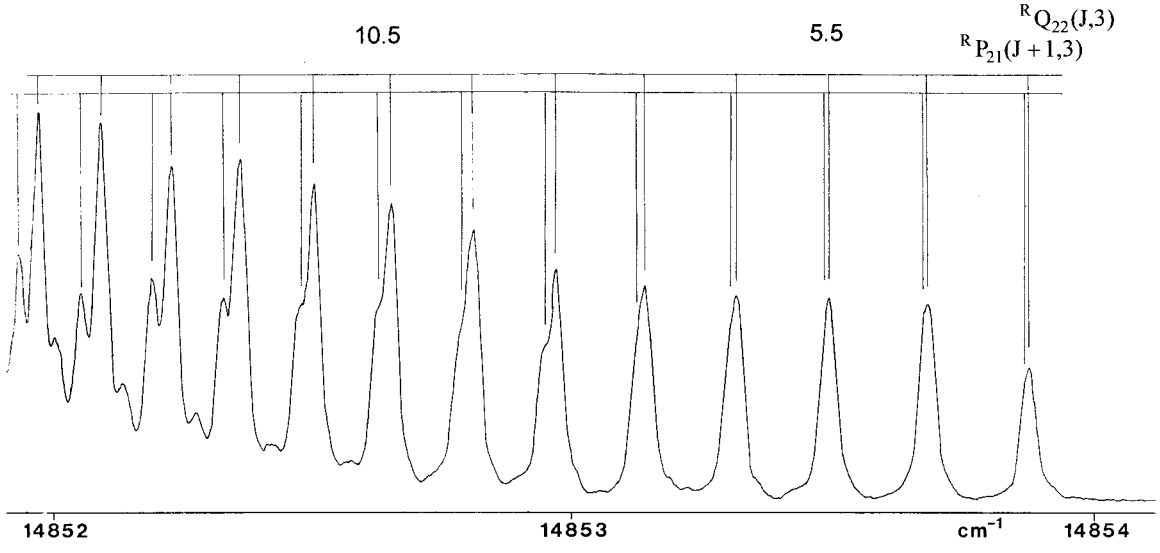

FIG. 4. The $-B$ branch of the 4–3 subband of the $\tilde{B}^2B_1$–$\tilde{X}^2A_1$ system of $SrNH_2$. The first line ($N'' = 4$, $J' = 3.5$) identifies this subband as having effective orbital angular momentum of $K'_a - 0.5$, for the $\tilde{B}^2B_1$ state. This is the F_2 or higher energy component. Some lines coming back from the bandhead can also be seen. The spectrum was recorded by scanning the laser and recording fluorescence in the corresponding 4–5 subband, which may have affected the relative intensities somewhat. The branches are identified as ${}^{\Delta K_a}\Delta J_{F'F''}(J'', K''_a)$.

found or could not be fitted to an asymmetric-rotor Hamiltonian. Some subbands of the correct K_a were found in approximately the right region, but the ground state rotational constants did not match, suggesting that these were from hot bands. It was concluded that the $\tilde{B}^2B_1$ state of $SrNH_2$ is perturbed, most likely by the $\nu_3 = 1$ (one quantum of the Sr–N stretch) level of the $\tilde{A}^2B_2$ state. The ν_3 mode in the two states where it could be measured ($\tilde{X}^2A_1$ and $\tilde{C}^2A_1$) has almost exactly the same frequency as the separation between the $\tilde{A}^2B_2$ and $\tilde{B}^2B_1$ states.

As the large extent of the perturbations in the $\tilde{B}^2B_1$ state made a full rotational analysis very difficult, a decision was made to analyze the $\tilde{A}^2B_2$–$\tilde{X}^2A_1$ transition. With the experience gained in recording the $\tilde{B}^2B_1$–$\tilde{X}^2A_1$ system, it was relatively easy to record all the subbands with K'_a up to 4 in the 0_0^0 band of the $\tilde{A}^2B_2$–$\tilde{X}^2A_1$ system of $SrNH_2$. As was the case with the $\tilde{B}$–$\tilde{X}$ system, the strong clear bandheads were on the red end of the low-resolution spectrum, indicating that this was where the 0_0^0 subbands were located, with the broad hump to the blue (see Fig. 1) due to sequence structure. Analysis of the 0–1 and 1–0 subbands, where transitions only occur to one of the asymmetry components in the $K_a = 1$ levels, showed that the selection rule on K_c was $\Delta K_c = \pm 1, \pm 3$. Hence this transition is B_2–A_1 and the transition dipole moment is along the b symmetry axis.

The subbands without asymmetry doubling were initially fit using a standard ${}^2\Pi$–${}^2\Sigma$ Hamiltonian. This was useful for checking the line assignments and obtaining preliminary constants. To analyze all of the bands together, a computer program was developed using a full-doublet asymmetric-rotor Hamiltonian. The standard A-reduced form of Watson's Hamiltonian (*21*) was used together with the spin–rotation Hamiltonian from Brown and Sears (*22*). Matrix elements for this Hamiltonian are given by Hirota (*23*). Matrix elements for additional centrifugal distortion terms were developed by multiplying the appropriate matrices for the lower order terms. There are no terms connecting odd and even K_a so these two sets of levels were calculated separately. A parity transformation of the matrix was also performed to reduce the size of the matrices. As the $\Delta K_a = \pm 2$ terms were included, all of the matrices were of order $J \times J$ and for higher J were very slow to diagonalize. For the ground state it was possible to truncate the matrices at $K_{\max} + 4$, or $K = 9$. The large off-diagonal spin–rotation terms in the excited states required terms out to $K_{\max} + 8$ or $K = 12$ before there was no further change in the energies when adding more terms. The $\tilde{A}^2B_2$–$\tilde{X}^2A_1$ subbands were initially fitted separately to the asymmetric-rotor Hamiltonian and then all of the bands were fitted together. For the final fit of the $\tilde{A}^2B_2$–$\tilde{X}^2A_1$ band 3771 lines covering K_a up to 4 in the $\tilde{A}^2B_2$ state and K_a up to 5 in the $\tilde{X}^2A_1$ state were fitted to a total of 41 parameters. The parameters determined are given in Table 2.

Fitting of the $\tilde{B}^2B_1$–$\tilde{X}^2A_1$ data was much more complicated due to the extensive perturbations. The precise ground state energy levels from the $\tilde{A}^2B_2$–$\tilde{X}^2A_1$ system were used to confirm that the subbands were part of the 0_0^0 band. The subbands involving the least-perturbed excited state levels $K_a = 2$, 4, and 1e were fitted together keeping the ground state constants fixed to the values from the $\tilde{A}$–$\tilde{X}$ analysis. The results of this fit are also given in Table 2. The output data from both fits are available as supplementary data from the Journal or from the authors on request. Additional listings of perturbed and hot

TABLE 2
Rotational Constants for $SrNH_2$ (in cm^{-1})

Constant	$\tilde{X}^2A_1$	$\tilde{A}^2B_2$	$\tilde{B}^2B_1$
T_{00}	0	14230.6237(3)[a]	14689.3234(4)
A	13.142570(78)	12.10285(12)	14.71405(13)
B + C	0.4485747(77)	0.4567744(77)	0.4554687(19)
B − C	0.0045208(73)	0.0046543(96)	0.0043801(49)
$10^7 \times \Delta_J$	1.934(26)	1.878(27)	1.8339(36)
$10^5 \times \Delta_{JK}$	4.5309(77)	3.279(12)	4.923(12)
Δ_K	0.0022682(26)	0.001878(27)	0.002[b]
$10^9 \times \delta_J$	5.01(14)	3.35(34)	3.28[b]
$10^5 \times \delta_K$	3.92(18)	1.29(21)	
$10^{12} \times H_{JK}$	−2.57(57)	−2.84(58)	−2.8[b]
$10^9 \times H_{JK}$	1.213(31)	0.479(40)	1.023(44)
$10^7 \times H_{KJ}$	−3.007(21)	−1.351(47)	
$10^5 \times H_K$	−0.160(20)	−2.124(77)	
ε_{aa}	0.00293(37)	30.01872(22)	−33.35915(45)
$\varepsilon_{bb} + \varepsilon_{cc}$	0.004687(25)	0.310337(85)	0.31064(59)
$\varepsilon_{bb} - \varepsilon_{cc}$	−0.001077(28)	−0.235467(52)	0.0550(15)
$10^7 \times D_{JS}$	0.570(67)	4.80(57)	2.91(92)
$10^4 \times D_{KJS}$	−0.0276(58)	3.28(13)	87.79(85)
D_{KS}		−0.144924(49)	0.53084(14)
$10^8 \times \delta_{JS}$		-4.1(11)	
$10^4 \times \delta_{KS}$		−0.382(37)	4.897(38)
$10^{11} \times H_{JS}$		−7.9(17)	
$10^8 \times H_{JKJS}$		−9.97(77)	
$10^4 \times H_{KS}$		5.346(25)	

[a] One standard deviation error estimate from the least squares analysis

[b] Held fixed

band data for the $\tilde{B}^2B_1$–$\tilde{X}^2A_1$ system which were not included in the final fit may be obtained from the authors.

DISCUSSION

The $\tilde{A}^2B_2$ and $\tilde{B}^2B_1$ states of $SrNH_2$ interact strongly with each other. This is a Coriolis-type interaction since the two states differ in symmetry by a rotation about the a axis. These two states correlate to the $\tilde{A}^2\Pi$ state in the isoelectronic SrOH molecule. The presence of the two hydrogen atoms in $SrNH_2$ breaks the symmetry of the two $p\pi$ orbitals in SrOH and they become localized along the p_x and p_y symmetry (or p_c and p_b rotational) axes of the molecule. This is an accurate picture of the unpaired electron when there is no rotational motion about the a axis; however, as soon as the molecule begins to rotate this picture breaks down. As the molecule rotates faster, the unpaired electron begins to slip and this leads to a mixing of the p_x and p_y orbitals.

As this orbital motion mixes with the unpaired spin it generates an effective spin–orbit splitting that initially increases linearly with K_a. For large enough K_a the unpaired electron is decoupled from the nuclear framework and the molecule is effectively like a symmetric top. This implies that the size of the spin splitting should reach a maximum value on the order of the spin–orbit splitting in the analogous linear molecule ($A = 264$ cm^{-1} for SrOH (*20*)). This significantly less than linear growth in the splitting can be seen in the experimental data for the $\tilde{A}^2B_2$ state shown in Fig. 5. The splitting for $K_a = 1$ is 29.4 cm^{-1}, while it only increases by

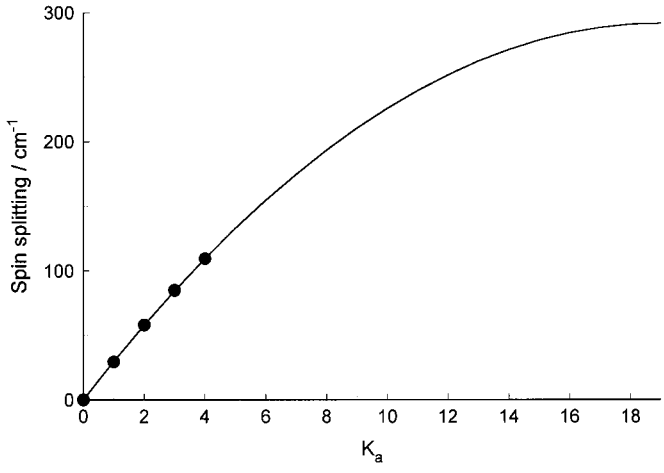

FIG. 5. Variation of the spin splitting in the $\tilde{A}^2B_2$ state of $SrNH_2$ with K_a. The splitting increases at a much less than linear rate, appearing to reach a plateau at high K_a. The circles are the observed splittings and the line is a fit to a function of the form $S(K_a) = S_{max} - a(K_{max} - K_a)^2$, where S is the splitting, S_{max} is the asymptotic splitting, K_{max} is the value of K_a at which this occurs, and a is an arbitrary parameter.

24.6 cm^{-1} from $K_a = 3$ to $K_a = 4$. The observed splittings $S(K)$ can be fitted to a simple asymptotic function

$$S(K_a) = S_{max} - a(K_{max} - K_a)^2$$

to obtain an estimate of the maximum splitting S_{max} which occurs at K_{max} with a single variable parameter a. A linear fit or higher order exponents do not adequately represent the data, while the limited amount of data available does not justify using additional variable parameters. The results of fitting of the observed data for $K = 0, \ldots, 4$ are given in Table 3. The estimated limiting splitting $S_{max} = 291 \pm 26$ cm^{-1} is reasonable compared to $A = 264$ cm^{-1} for SrOH (*20*) and $A = 296$ cm^{-1} for SrN_3 (*24*). It would be interesting to observe the higher K_a levels and see if a limiting splitting is indeed

TABLE 3
Fit of the Spin-Splitting $S(K_a)$ in the $\tilde{A}^2B_2$ State of $SrNH_2$

Parameter	Value
S_{max}	292(26)[a] cm^{-1}
K_{max}	19(2)
a	0.81(9)

[a] Values in parentheses are 1 std dev errors in the last figure

K_a	Observed $S(K_a)$	Calculated $S(K_a)$
0	0	-0.2
1	29.4	29.7
2	58.0	58.0
3	84.9	84.6
4	109.5	109.6

TABLE 4
Calculated Coriolis Interactions for $SrNH_2$ (in cm^{-1})

$\tilde{A}^2B_2$			
$\epsilon_{aa} = 30.3$	$A^{(2)} = 1.51$	$\epsilon_{cc} = 0.146$	$C^{(2)} = -0.00013$
$\tilde{B}^2B_1$			
$\epsilon_{aa} = -30.0$	$A^{(2)} = -1.51$	$\epsilon_{bb} = 0.207$	$B^{(2)} = -0.00018$
$\tilde{C}^2A_1$			
$\epsilon_{bb} = -0.207$	$B^{(2)} = 0.00018$	$\epsilon_{cc} = -0.146$	$C^{(2)} = 0.00013$

reached. Too few of the subbands in the $\tilde{B}^2B_1$–$\tilde{X}^2A_1$ system are unperturbed to permit a comparable analysis.

The Coriolis interaction between the $\tilde{A}^2B_2$ and $\tilde{B}^2B_1$ states also has a significant effect on the spacing of the K_a rotational levels for the two states. The true A rotational constant for each state is modified to an effective one that is 1.51 cm^{-1} smaller for the $\tilde{A}^2B_2$ state and 1.51 cm^{-1} larger for the $\tilde{B}^2B_1$ state. Explicit expressions for the interaction were derived by Whitham and Jungen (*11*) using second-order perturbation theory and by Morbi *et al.* (*14*) using a pure precession model. Both models give the following expressions for the second-order contributions to the ϵ_{aa} spin–rotation interaction and the A rotational constant

$$\epsilon_{aa}^{(2)} = \pm \frac{4AA_{SO}}{E_{\tilde{B}} - E_{\tilde{A}}}, \quad A^{(2)} = \mp \frac{4A^2}{E_{\tilde{B}} - E_{\tilde{A}}},$$

where the upper sign refers to the $\tilde{A}$ state and the lower sign to the $\tilde{B}$ state. Similar interactions occur with the $\tilde{C}^2A_1$ electronic state (T_{00} = 15 862 cm^{-1} from a low-resolution laser excitation scan) which correlates to the $\tilde{B}^2\Sigma^+$ state of linear SrOH. This affects the C and ϵ_{cc} constants for the $\tilde{A}^2B_2$ state and the B and ϵ_{bb} constants for the $\tilde{B}^2B_1$ state. The calculated corrections due to the Coriolis interactions between the three states are given in Table 4. The spin–orbit splitting for SrOH (A_{SO} = 264 cm^{-1} (*20*)) is used as the estimated value for the spin–orbit interaction in $SrNH_2$.

The calculated values for ϵ_{aa} in the $\tilde{A}^2B_2$ and $\tilde{B}^2B_1$ states match extremely well. This is to be expected as these states lie close together and hence their mutual interaction dominates the contribution to ϵ_{aa}. However, the good agreement does validate the simple treatment that was used. The contribution of the Coriolis interaction to the A rotational constants for the $\tilde{A}^2B_2$ and $\tilde{B}^2B_1$ states is also very substantial. When the observed spectroscopic constants are corrected for this interaction, the true values are found to be A = 13.61 cm^{-1} in the $\tilde{A}^2B_2$ state and A = 13.20 cm^{-1} in the $\tilde{B}^2B_1$ state. Both constants are now very similar to the $\tilde{X}^2A_1$ state value of A = 13.14 cm^{-1}. The geometry changes that would be implied by the original uncorrected constants are totally inconsistent with the strontium-centered nature of the electronic transition and the highly diagonal Franck–Condon factors.

The agreement for the ϵ_{bb} and ϵ_{cc} spin–rotation interactions is not as good as for ϵ_{aa} as can be seen in Table 4. For the $\tilde{A}^2B_2$ state ϵ_{bb} is predicted to be zero and it is indeed very small, but ϵ_{cc} is almost a factor of 2 larger than expected. For the $\tilde{B}^2B_1$ state ϵ_{bb} is again well predicted but ϵ_{cc} is relatively large when it is predicted to be zero. The experimental values for the $\tilde{B}^2B_1$ state should be treated with some caution as many of the K_a levels are badly perturbed and the ones analyzed, while not obviously perturbed, may be affected somewhat by smaller perturbations. The overall agreement is satisfactory and better than was found for $CaNH_2$ (*14*).

The corrections to the B and C rotational constants for both states are very small. The adjustment to C in the $\tilde{A}^2B_2$ state is 0.000125 cm^{-1} and to B in the $\tilde{B}^2B_1$ state is 0.000180 cm^{-1}. The inertial defect for the $\tilde{X}^2A_1$ state is found to be 0.2324 amu Å^2. This is a reasonable value for the $v = 0$ level of a planar molecule and results from the failure to correct the rotational constants to the equilibrium values. The inertial defects for the $\tilde{A}^2B_2$ and $\tilde{B}^2B_1$ states are 0.224 and 0.204 amu Å^2, respectively, very similar to the ground state. Without correction to the B and C rotational constants for the Coriolis interaction with the $\tilde{C}^2A_1$ state, the values would be 0.265 and 0.147 amu Å^2, respectively, quite different from each other and the ground state.

The centrifugal distortion constants for the $\tilde{X}^2A_1$ and $\tilde{A}^2B_2$ states are all reasonable and could be analyzed in terms of the molecular force field. The $\tilde{B}^2B_1$ state values, especially for the spin–rotation interaction, are affected by the perturbation and in many cases are just effective fitting parameters with no physical meaning.

There is insufficient data from the current experiment to obtain an r_0 geometry for $SrNH_2$ without making some assumptions. The B and C rotational constants are mainly determined by the Sr–N separation while the A rotational constant is determined by the N–H bond length and H–N–H angle. For the amide ion, NH_2^-, the N–H bond length is 1.041 Å (*25*). Using this value the H–N–H bond angle for $SrNH_2$ was found to be 100.0° in the $\tilde{X}^2A_1$ state. This is slightly smaller than for NH_2^-, although the difference is within the range of possible solutions given the inertial defects for the two species. All geometric parameters are listed in Table 5. While the absolute value for the bond angle is only good to a few degrees, the relative changes between the three states examined should be fairly precise. Using the same 1.041 Å bond length for the N–H bond length gives H–N–H bond angles of 97.7° and 99.7° for the $\tilde{A}^2B_2$ and $\tilde{B}^2B_1$ states, respectively, using the A rotational

TABLE 5
Experimental Geometry for $SrNH_2$ with N–H Bond Length Fixed at 1.041 Å

	$\tilde{X}^2A_1$	$\tilde{A}^2B_2$	$\tilde{B}^2B_1$
Sr–N bond length	2.247 Å	2.223 Å	2.228 Å
H–N–H bond angle	100.0°	97.7°	99.7°

constants corrected for the Coriolis interaction. The $\tilde{B}^2B_1$ state value is essentially unchanged from the $\tilde{X}^2A_1$ state while the $\tilde{A}^2B_2$ state value is significantly smaller. This is consistent with the $\tilde{B}^2B_1$ state being due to a promotion of a strontium-centered electron from the 5*s* orbital to the out-of-plane 5*p* orbital, while the electron is promoted to the in-plane 5*p* orbital in the $\tilde{A}^2B_2$ state. Repulsion due to the in-plane strontium 5*p* electron leads to a reduction in the H–N–H bond angle.

The Sr–N bond length is found to be 2.247, 2.223, and 2.228 Å for the $\tilde{X}^2A_1$, $\tilde{A}^2B_2$, and $\tilde{B}^2B_1$ states, respectively. The ground state bond length is very similar to other strontium species such as SrN_3 (*24*) and SrNCO (*26*), both of which were found to have Sr–N bond lengths of 2.26 Å. This is somewhat longer than the corresponding oxygen-bonded species SrOH for which a bond length of 2.11 Å was found (*20*). The slight shortening of the Sr–N bond on excitation to the $\tilde{A}^2B_2$ and $\tilde{B}^2B_1$ states is also found in the corresponding $^2\Pi$ states of the linear species SrOH (*20*), SrN_3 (*24*), and SrNCO (*26*).

CONCLUSION

We observed the $SrNH_2$ molecule at high resolution for the first time. Both the $\tilde{A}^2B_2$–$\tilde{X}^2A_1$ and $\tilde{B}^2B_1$–$\tilde{X}^2A_1$ systems were observed, although analysis of the $\tilde{B}^2B_1$–$\tilde{X}^2A_1$ system was hampered by extensive systematic perturbations of some subbands. Extremely large spin–rotation splittings in the $\tilde{A}^2B_2$ and $\tilde{B}^2B_1$ states caused all of the subbands except those with $K'_a = 0$ to split into two components with rotational structure similar to a Hund's case (a) $^2\Pi$–$^2\Sigma^+$ transition of a linear molecule.

REFERENCES

1. P. F. Bernath, *Science* **254,** 665–670 (1991).
2. P. F. Bernath in "Advances in Photochemistry," (D. C. Neckers, D. H. Volman, and G. Von Bunau, Eds.) Vol. 23, Chap. 1, Wiley-Interscience, New York, 1997.
3. C. R. Brazier and P. F. Bernath, *J. Chem. Phys.* **91,** 4548–4554 (1989).
4. L. C. O'Brien, C. R. Brazier, and P. F. Bernath, *J. Mol. Spectrosc.* **130,** 33–45 (1988).
5. C. J. Whitham, S. A. Beaton, Y. Ito, and J. M. Brown, *J. Mol. Spectrosc.* **191,** 286–294 (1998).
6. C. N. Jarman and P. F. Bernath, *J. Chem. Phys.* **98,** 6697–6703 (1993).
7. C. T. Scurlock, T. Henderson, S. Bosely, K. Y. Jung, and T. C. Steimle, *J. Chem. Phys.* **100,** 5481–5490 (1994).
8. R. F. Wormsbecher, M. Trkula, C. Martner, R. E. Penn, and D. O. Harris, *J. Mol. Spectrosc.* **97,** 29–36 (1983).
9. R. F. Wormsbecher, R. E. Penn, and D. O. Harris, *J. Mol. Spectrosc.* **97,** 65–72 (1983).
10. C. J. Whitham, B. Soep, J-P. Visticot, and A. Keller, *J. Chem. Phys.* **93,** 991–1000 (1990).
11. C. J. Whitham and Ch. Jungen, *J. Chem. Phys.* **93,** 1001–1008 (1990).
12. A. J. Marr, M. Tanimoto, D. Goodridge, and T. C. Steimle, *J. Chem. Phys.* **103,** 4466–4475 (1995).
13. Z. Morbi, C. Zhao, J. W. Hepburn, and P. F. Bernath, *J. Chem. Phys.* **108,** 8891–8898 (1998).
14. Z. Morbi, C. Zhao, and P. F. Bernath, *J. Chem. Phys.* **106,** 4860–4868 (1997).
15. J. V. Ortiz, *J. Chem. Phys.* **92,** 6728–6731 (1990).
16. A. M. R. P. Bopegedera, C. R. Brazier, and P. F. Bernath, *J. Phys. Chem.* **91,** 2779–2781 (1987).
17. J. B. West, R. S. Bradford, Jr., and C. R. Jones, *Rev. Sci. Instrum.* **46,** 164–168 (1975).
18. S. Gerstenkorn and P. Luc, "Atlas du Spectre d'Absorption de la Molecule d'Iode," Laboratorie Amie-Cotton, Presses du CNRS, Paris, France.
19. S. Gerstenkorn and P. Luc, *Rev. Phys. Appl.* **14,** 791–796 (1979).
20. C. R. Brazier and P. F. Bernath, *J. Mol. Spectrosc.* **114,** 163–173 (1985).
21. J. K. G. Watson, *J. Chem. Phys.* **46,** 1935–1949 (1967).
22. J. M. Brown and T. J. Sears, *J. Mol. Spectrosc.* **75,** 111–133 (1979).
23. E. Hirota, "High-Resolution Spectroscopy of Transient Molecules," Springer Series in Chemical Physics, Vol. 40, Springer-Verlag, Berlin, 1985.
24. C. R. Brazier and P. F. Bernath, *J. Chem. Phys.* **88,** 2112–2116 (1988).
25. L. M. Tack, N. H. Rosenbaum, J. C. Owrutsky, and R. J. Saykally, *J. Chem. Phys.* **84,** 7056–7057 (1986).
26. L. C. O'Brien and P. F. Bernath, *J. Chem. Phys.* **88,** 2117–2120 (1988).